DES of the Flow Around a Realistic Bus Model Subjected to a Side Wind with 30^o Yaw Angle

HASSAN HEMIDA
Chalmers University of Technology,
Department of Applied Mechanics
SE 412 96 Gothenburg
SWEDEN

SINIŠA KRAJNOVIĆ
Chalmers University of Technology,
Department of Applied Mechanics
SE 412 96 Gothenburg
SWEDEN

Abstract: Detached-Eddy Simulation (DES) was made for the flow around a 1/10 model of a double-deck bus of the type Scania K112 TL. The bus was subjected to a side wind with 30^o yaw angle. The Reynolds number of the flow, based on the speed of the side wind and a reference length of $\sqrt{0.1}$ [m], was 1.3×10^6. Detailed flow structures and global quantities such as lift, drag, side force, yaw moment and pressure coefficients were computed. Visualizations of time-averaged and instantaneous flow structures showed that the flow separates on the top and the lee-side faces of the bus. The flow separations on the lee-side face of the bus was found to be unsteady yielding large vortices that shed to the wake flow leaving disturbances on the surface pressure and hence the side force. The flow separation on the top-side face was found to be more stable in the first two third of the bus length. It became unsteady three-dimensional vortex shedding in the last one third of the length of the bus. The flow under the neath of the bus was found to be very complex and was dominated with small vortices shedding from the beams and the wheels of the bus. Good agreement was found between the DES results and the available experimental data.

Key–Words: DES, Side wind, Vehicles aerodynamics, Flow structures, Unsteady flow.

1 Introduction

A bus in motion is subjected to different aerodynamic forces such as drag, lift and side force and aerodynamic moments such as yaw, rolling and pitch moments. These forces and moments depend very much on the relative wind speed and the direction of the wind relative to the bus-the yaw angle. In case of strong side wind, the side force and the lift force might be large enough to deviate or turn over the bus. Recently, due to decrease of vehicles weight, the research in the field of the flow structures around vehicles have increased. Several research papers have addressed the stability of high-speed trains subjected to side winds [1–7]. Some other papers have addressed the side wind flow around ground vehicles [8–11] However, only few publications deal with the subject of flow structures around buses subjected to side winds.

Due to strong winds in Sweden, especially in the winter, there is a high risk of bus accidents [12]. In November 1998, between Enköping and Sala, a bus has turned over and six people were killed. This accident has led to a study of the cross-wind stability characteristics of this bus. This study has been done by the Swedish defense research agency (FOI), previously called the aeronautical research institute of Sweden (FFA). They have investigated experimentally the aerodynamic coefficient around a model bus subjected to a side wind with yaw angles ranges from -95^o to $+95^o$ [13]. They have found that the most critical side wind yaw angle is 30^o where the lift force and the yaw moment coefficients are maximum. Moreover, for yaw angles more than 30^o, the value of the side force and the rolling moment coefficients are no longer sensitive to any change of the yaw angle. The main aim of the experimental work was to measure the time-averaged values for the aerodynamic coefficients. However, no effort was done to understand the flow field around the bus.

In this paper, the flow around a double-deck bus model, subjected to side wind with a 30^o yaw angle, has been computed using Detached-Eddy Simulation (DES). The bus is a 1/10 model of the type Scania K112 TL. High level of complexities have been maintained in the geometry, especially in the under body, in order to simulate the realistic flow conditions. The Reynolds number of the flow, based on the speed of the relative side wind and a reference length of $\sqrt{0.1}$ [m], is 1.3×10^6. The results have been compared with the experiment in [13] and good agreement has been obtained. This paper explores the time-averaged and the instantaneous flow structures around the bus as well as the time variation of the aerodynamic coefficients.

2 Set-up and boundary conditions

The bus used in this paper is a 1/10 model of a double-deck bus of the type Scania K112 TL. The model has some geometrical details under the neath of the bus such as wheels,

beams and axles as shown in Fig. 1. This model has been used for the experimental investigation of the sensitivity of side winds using different yaw angles. Low-speed wind tunnel experiments have been done for the range of yaw angles between -95^o and +95^o at two different Reynolds numbers of 1.3×10^6 and 1.6×10^6, based on the speed of the side wind and a reference length of $\sqrt{0.1}$ [m] [13]. The experiment, based on the higher Reynolds number, has been done to investigate the influence of the Reynolds number on the aerodynamic coefficients which has verified the fact that the aerodynamic coefficients are Reynolds number independent or, in other words, the effect of the Reynolds number is very low. The height of the bus is $H = 400$ mm and the length is $L = 1190$ mm while its width at the widest part is $W = 300$ mm. To simulate the under neath of the real bus, pipes of 12 mm diameter are drilled in the chassis of the bus to connect the two sides of the wheel houses. These pipes allow the air to pass from one side to the other.

Similar to the experiment, the model has been mounted on the floor of the wind tunnel as shown in Fig. 2. The cross section of the wind tunnel is circular with diameter 3600 mm as shown in Fig. 2.a. The center of the model is lowered 300 mm dawn from the center of the tunnel to reduce the blockage ratio. The distance between the inlet section of the wind tunnel and the face of the bus, in our simulation, is $8H$ which is about $2H$ longer than that of the experiment. The purpose of this longer distance is to make sure that the inlet pressure will not be influenced by the model. This constrain is essential for the numerical stability. The boundary layer thickness on the floor has been measured in the experimental work at the model reference point (midway between the front and second axles) to be 37 mm. It has been measured while the model has not been mounted in the channel. This boundary layer thickness has been used for the estimation of the upstream length of the no slip floor in the computational domain. The remaining length of the upstream floor is used as slip floor (see Fig. 2.b where no boundary layer is formed. The estimated length of the no-slip upstream distance, based on the turbulent boundary layer theory over a flat plate, has been found to be equal to that of the upstream distance of the floor in the experiment.

Uniform inlet velocity, constant in time, with 0.25% turbulent intensity has been used at the inlet of the domain. Wall function boundary conditions are used on the model, floor, and on the wind tunnel walls. This boundary condition has been implemented in Fluent6.2 to switch between the linear viscous layer law and the turbulent logarithmic wall law based on the resolution normal to the wall, y^+. In case of $y^+ < 11.5$ it uses the linear sublayer law to calculate the shear stress at the first cell close to the wall and pure no-slip boundary condition is retained. In case of $y^+ > 30$ the standard wall function is used to calculate the shear stress at the first cell close to the wall based on

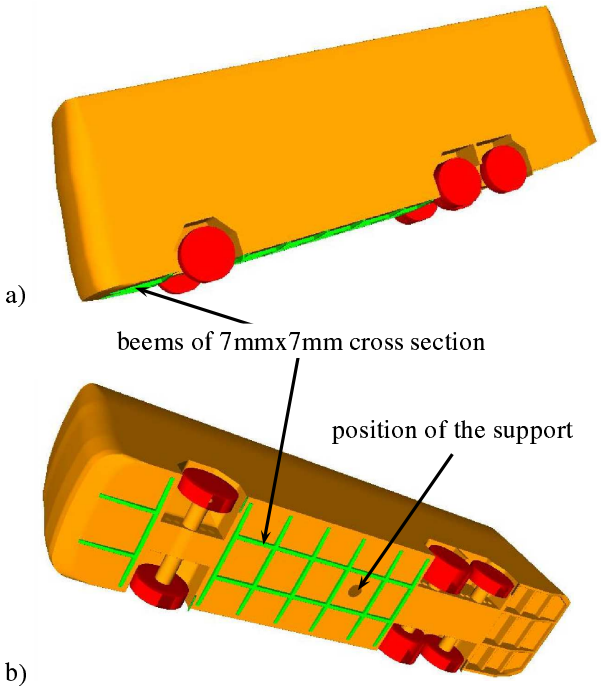

Figure 1: The shape of the bus model: (a) view from the side and front, (b) view from the bottom of the bus showing the beams, the wheels and the axles.

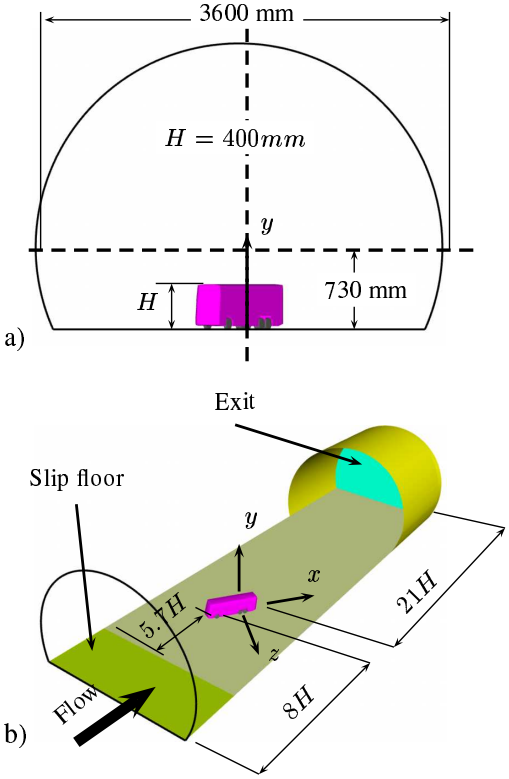

Figure 2: Computational domain: (a) cross section of the tunnel, (b) the dimensions of the computational domain.

the turbulent logarithmic wall law. On the other hand, if $11.5 < y^+ < 30$ then some kind of blending between the linear law and the logarithmic law is used to find the shear

stress at the first cell close to the wall. Outlet boundary condition is used at the domain exit. This boundary condition implies Neumann boundary condition for all the variables in the normal direction to the outlet section.

3 Numerical Method

The side wind flow around the bus was solved using Detached-Eddy Simulation (DES). The governing equations have been averaged over a small time interval which is the discretized time step. Due to the averaging process, an extra term has appeared in the averaged Navier-Stokes equations representing the turbulent stresses. For the DES, the commercial CFD-code, Fluent6.2, has been employed. In Fluent6.2, the closure model in DES is based on a modification of the Spalart-Allmaras one-equation model [14]. The standard Spalart-Allmaras model solves a transport equation for a modified eddy viscosity. The length scale used in this model is the distance between the center of the computational cell and the nearest wall. The modification to the Spalart-Allmaras model to obtain the DES formulation is redefinition of the minimum wall distance d with a new length scale, $d = min(d, C_{DES}\Delta)$ where Δ is the local maximum grid spacing in the three directions. Near solid boundaries, Δ is larger than d, the standard Spalart-Allmaras model is recovered, and the flow is predicted from the Reynolds-averaged equations. Far from walls, $\Delta < d$ and a balance between the production and destruction terms in the model equation shows that the definition for the closure model is similar to a Smagorinsky-like expression for the eddy viscosity in the 'LES region' [15]. The length scale redefinition increases the magnitude of the destruction term in the Spalart-Allmaras model, drawing down the eddy viscosity and allowing instabilities to develop, creating a cascade down to the grid scale as in classical LES. A constant value of 0.65 has been used for the model coefficient, C_{DES}. Constantinescu and Squires [15] have showed that the model is very sensitive to the value of the model coefficient C_{DES} and the optimum value that retains results similar to those from the LES results is 0.65.

4 Mesh and numerical details

The ICEM-CFD package has been used to generate hexahedral mesh around the model. The mesh consists of $O-grid$, $C-grid$ and $H-grid$ topologies. Figure 3.a shows the mesh shape at the inlet of the computational domain. It consists of a $C-grid$ shape starting from the floor on one side of the bus and ends on the floor on the other side of the bus. Using a $C-grid$ topology in this part of the domain enables good quality cells close to the wind tunnel wall. This also helped to make finer meshes close to the model surface and close to the wind tunnel surface as a requirement for using no-slip boundary conditions on both surfaces. The mesh under the bus and around the wheels is very complex. It consists of combination of $C-grid$, $O-grid$ and $H-grid$ topologies. The grid topology around the axles and the wheels of the bus is mainly of the $C-grid$ type while grid topology in the part confined between the axles and the floor is of the $H-grid$ type. These topologies are connected with $O-grids$ in the small pipes connecting the two sides of the wheel houses as shown in Fig 3.b. The total number of nodes is about seven million, most of them is concentrated around the bus.

The momentum equation has been discretized using second-order bounded central difference scheme while the transport equation for the turbulent viscosity in Spalart-Allmaras model has been discretized using first order upwind scheme. Time discretization has been approximated using the second order Crank-Nicolson scheme. Constant time step, $\Delta t = 0.0001$ [sec] is used in the simulation. The maximum CFL number based on this time step, the inlet velocity and the height of the bus, H, is 5 while the mean value in the whole domain is lower than 0.5. The solution is initialized by the inlet velocity everywhere. The time history of the aerodynamic coefficients as well as the residual of all the turbulent variables have been monitoring in each time step during the simulation. Fully converged turbulent flow has been obtained in the domain after about seven thousand time steps. In each time step, the maximum residual of each turbulent equation has been converged to 10^{-4}. In fluent6.2, the residual is normalized by $\sum_{allnodes} a_p\phi_p$, where $a_p\phi_p$ is the left hand side of the discretized equation in finite volume method.

5 Results

In this section, the flow structures and the aerodynamic coefficients obtained from the DES of the side-wind flow around the model bus are explored in both time-averaged and instantaneous flow. The model is yawed by a 30^o yaw angle with respect to the relative side wind. The time-averaged flow is obtained using 42000 time steps or 0.42 [sec] total sampling time. This is equivalent to about 150 times one fluid particle passes over the entire length of the bus.

5.1 Time-averaged flow

The conventional directions for the drag force, left force, side force and yaw moment coefficients are shown in Fig. 5. The reference point of the yaw moment coefficient is located at the floor midpoint between the front and the back axles at the center of the supporting cylinder.

The time-averaged values for the aerodynamic coefficients are shown in Fig. 4 accompanied with the minimum and maximum peaks during the sampling time. All the aerodynamic coefficient are normalized with the den-

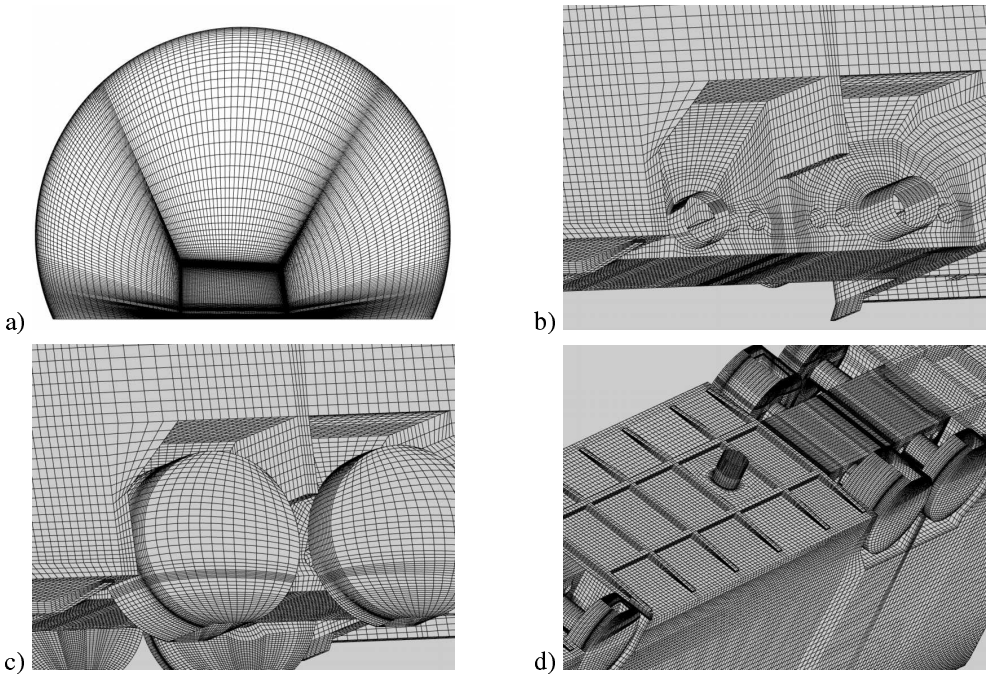

Figure 3: The computational mesh: (a) the mesh shape at the inlet plane, (b) the mesh shape around the axles, (c) the mesh around the wheels and (d) the mesh around the beams and the support.

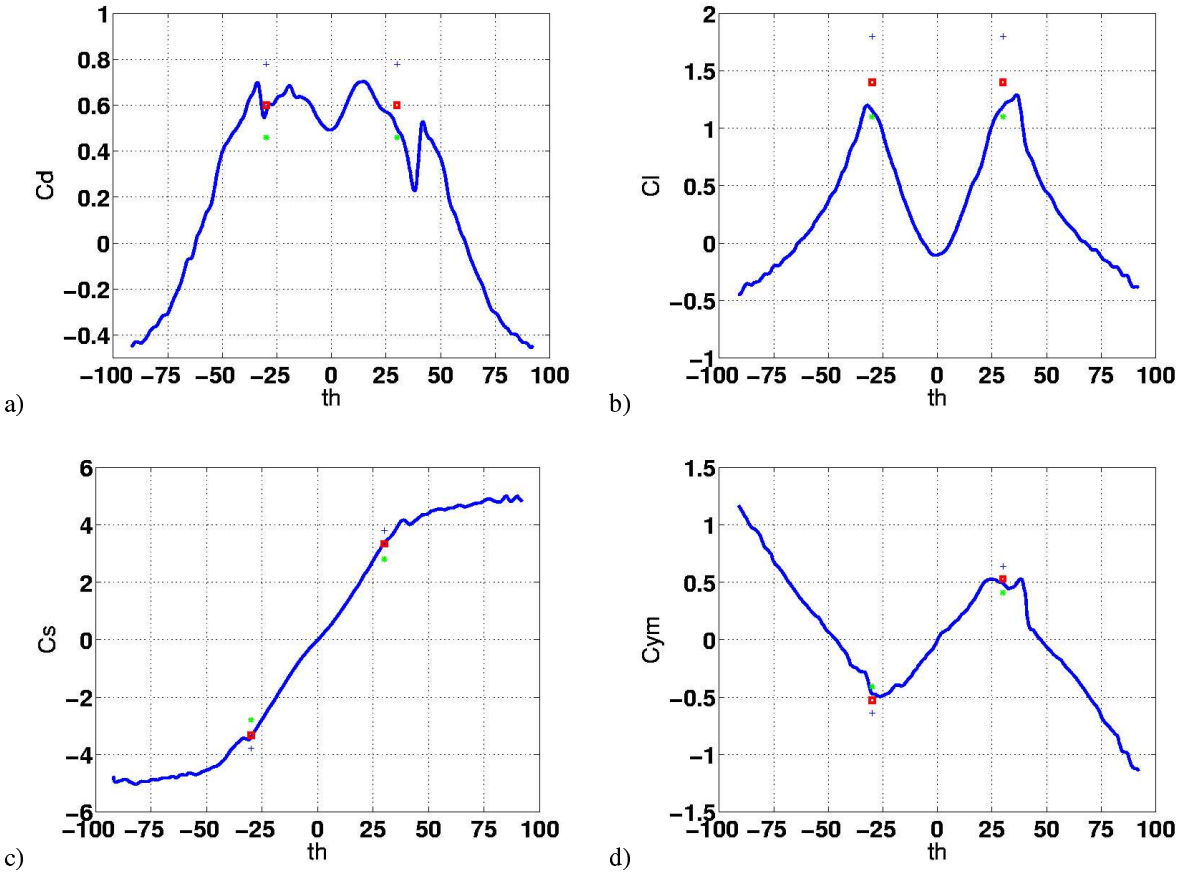

Figure 4: Comparison of the DES aerodynamic coefficients (symbols) and the experiment (solid lines): (a) drag coefficient, (b) lift coefficient, (c) side force coefficient and (d) yaw moment coefficient

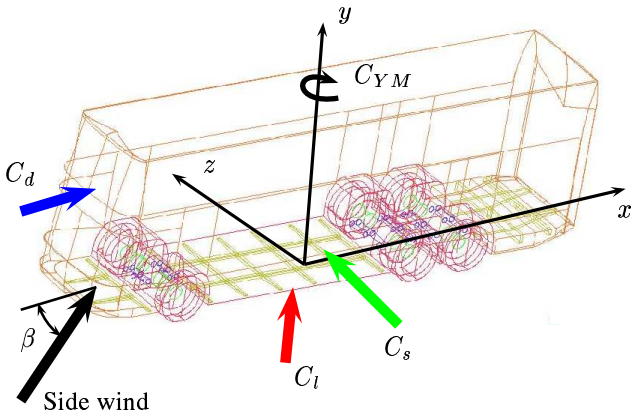

Figure 5: Conventional directions for the aerodynamic coefficient with respect to the side-wind direction.

sity of the air, $\rho = 1.16kg/m^3$, the free stream velocity $U_\infty = 57m/s$, reference area $A = 0.1m^2$ and reference length of one meter. Figure 4 shows the experimental vales for the aerodynamics coefficient at the range of yaw angles, β, between -95^o and +95^o. The computed values for the time-averaged side-force coefficient, C_s and the yaw-moment coefficient, C_{YM} agree well with the experimental values as shown in Fig. 4.c and d. Some discrepancies have been found between the computed time-averaged value for the drag coefficient, C_d and the experimental value. On the other hand, the difference in lift force coefficient, C_l, between the simulation and the experiment is relatively large as shown in Figs. 4.b. However, the measured values lye in between the maximum and minimum peaks for the computed aerodynamic coefficients. In the experiment, the model was moved continuously around the support cylinder at a rate of one angle per second. The aerodynamic coefficients have been computed using 100 samples at each angle. The model has been rotating continuously meaning that the 100 samples were not taken at constant yaw angle. The flow around the model, especially in the wake behind the bus, is not stationary, which raises a question about the credibility of the experimental data. Figure 4 shows that the curves obtained from the experiment are not symmetric around the zero yaw angle. This means that the continuous rotation of the model leaves some influences on the measured values. The drag-coefficient, C_d, that depends mainly on the wake structures behind the bus, seems to be affected very much by the rotation of the model. Moreover, the model in the experiment was raised 5 mm from the floor to allow its vibration and also to prevent any contribution of the friction between the wheels and the floor in the aerodynamic coefficients. The discrepancy in the lift force coefficient, C_l can be addressed to this 5 mm clearance and also to the possible vibration of the model. These vibrations might change the incidence angle of the coming air with respect to the bottom surface of the bus and hence the value of C_d. The distribution of the time-averaged local pressure coefficient, C_p, on the surface of the bus is shown in Fig. 6. The minimum surface pressure is found to be in the lee-side face of the bus close to the leading edge while the highest pressure is found to be on the edge between the front face of the bus and the upstream-side face of the bus. The highest time-averaged pressure on the lee-side face is confined between the front wheel and the back wheel in the middle of the height of the bus. Regions of higher and lower pressures are found on the top-side face of the bus as shown in Fig. 6.a.

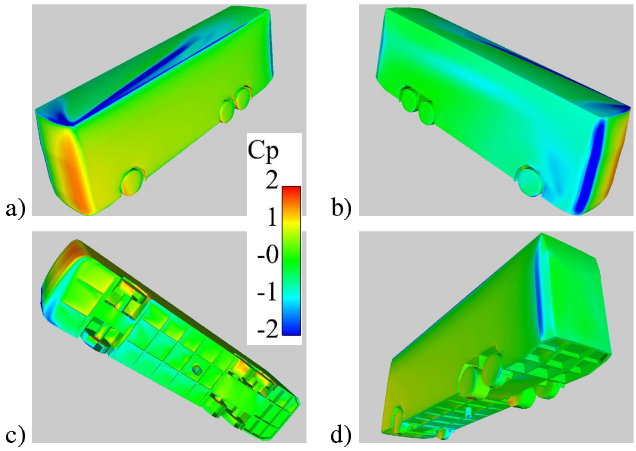

Figure 6: Distribution of the time-averaged pressure coefficient on the surface of the bus.

Figure 7 is a plot of the time-averaged local pressure coefficient, C_p along a line drown at the middle of the bus at $z = 0$ as shown in Fig. 7.a. There is high pressure on the front faces of the beams under the body of the bus and low pressures behind them as shown in Fig. 7.b as wiggle in the curve of local pressure coefficient.

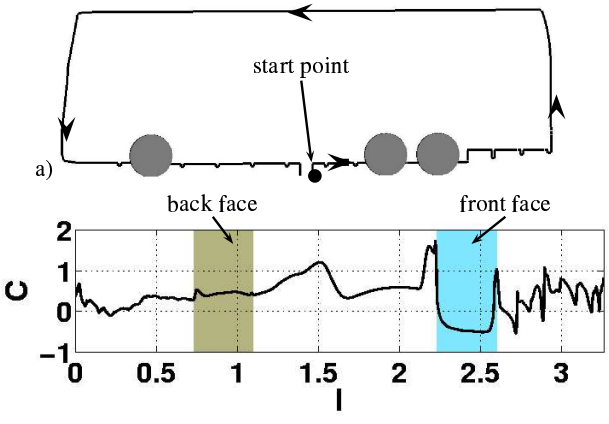

Figure 7: Local pressure coefficient: (a) the line along which the pressure coefficient is drawn showing the starting point and (b) the pressure coefficient against the length of the line.

Ensight software package is used to visualize the flow. Figure 8 shows the time-averaged flow structures around the bus by means of the vortex core technique. The side-

wind flow is completely attached to the front face and the upstream face of the bus. It separates at different places on the top-side face as shown in Fig 8.a. It separates at the front edge to form the vortex $Vc1$. It separates also at the upstream edge to form the vortex $Vc2$ and it reattaches to the surface before it separates again to form the strong separation vortex $Vc3$. The reattached flow in the top-side face separates from the surface at the lee-side edge to form the lee-side vortices. The lee-side flow structures are very complex containing different regions of flow separations and reattachments. The small vortex $Vc4$, shown in Fig. 8.c is formed at the top-side edge. The flow reattaches to the lee-side surface before it separates to form the lee-side recirculation bubble $Vc6$. The circulated flow in this vortex separates from the lee-side surface to form the separation vortex $Vc5$ before it meets with the reattached flow coming from the vortex $Vc4$. The vortex sheet from the under body flow rolls up to form the lower part of the recirculation region on the lee side, $Vc7$. Figure 8.c shows that the upper

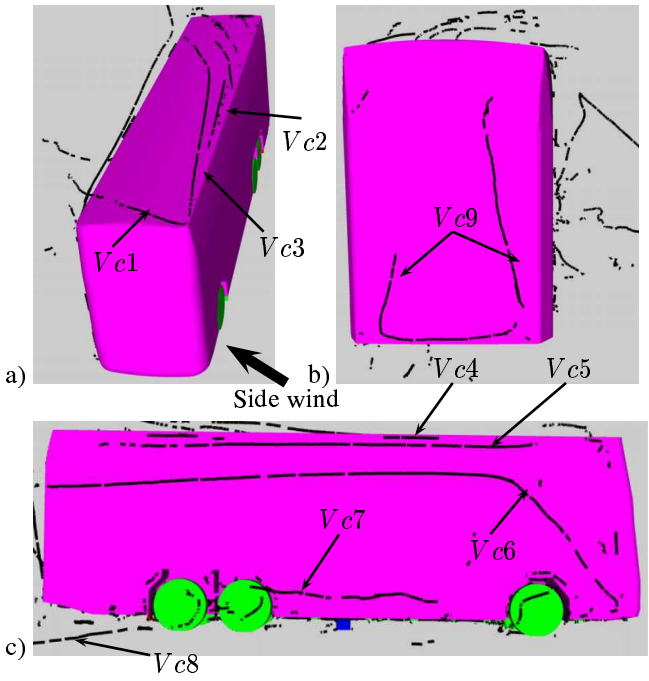

Figure 8: Vortex cores showing the time-averaged flow structures around the bus: (a) top-side face vortices, (b) back-side face vortices and (c) the lee-side face vortices.

recirculation bubble in the lee-side flow, $Vc6$, starts at the lower front corner of the lee-side face and extends along the whole bus length. On the other side, the lower recirculation bubble, $Vc7$, extends only between the front and the back wheels. The coming flows from the wheel houses to the lee-side flow destroy the extension of this bubble along the length of the bus. Figure 8.c shows a vortex, $Vc8$, close to the floor of the domain. This vortex is a swirling vortex formed due to the interaction between the free-stream flow and the flow from the back wheel house. The upstream flow, the lee-side flow and the underbody flow separate when they reach the back surface of the bus to form the wake flow. The time-averaged structures of the near wake flow is shown in Fig. 8.b as an upside-down arch shape vortex. We have found that several vortices are formed under the body of the bus, especially behind the beams, the supporting cylinder, in the wheel house and around the wheels of the bus.

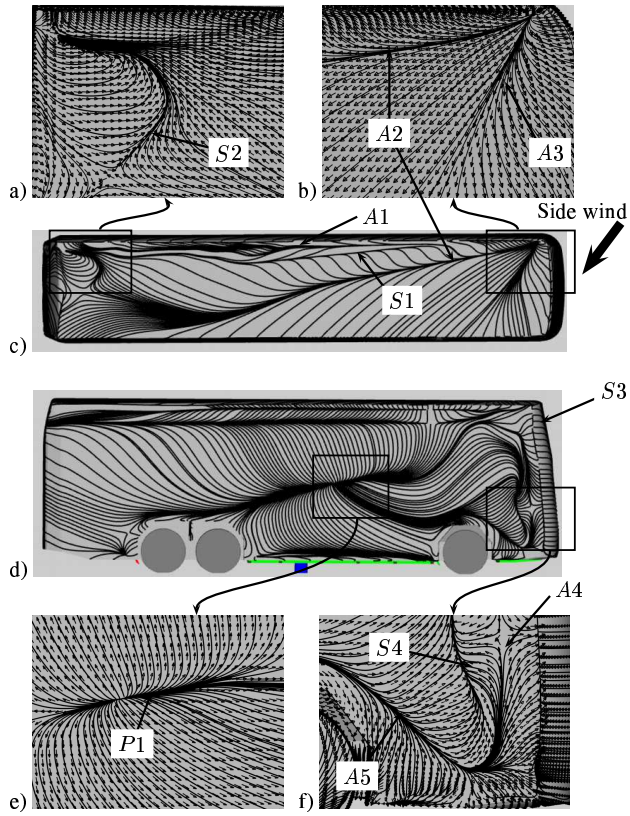

Figure 9: Time-averaged flow imprint on the top and lee-side face of the bus: a) and b) zoom in two critical regions in Fig. 9.c showing the direction of the flow while (e) and (f) zoom in two different regions in Fig. 9.d

Figure 9 shows the flow imprint on the surface of the bus. These flow patterns are the result of the flow structures in Fig. 8. Figure 9.c shows the reattachment line, $A1$ for the coming flow from the vortex $Vc2$ while $S1$ represents the separation line of the vortex $Vc3$ and $A2$ is the reattachment line for the same separation vortex. The flow separates at the front-face edge and forms the vortex $Vc1$ before it reattaches to the surface at the reattachment line $A3$. The coming flow from the separation vortex $Vc2$ on the top-side face interacts with the wake flow behind the bus to form the upside-down arch shape vortex behind the bus, $Vc9$. This vortex starts at the separation line $S2$ shown in Fig. 9.a. Figure 9.f shows the separation line, $S4$, and the reattachment line, $A5$ of the recirculation vortex $Vc6$. The figure also shows a small separation bubble in the lee-side flow starting with a separation line at the front edge of

the face and ending with the reattachment line $A4$. Figure 9.e shows the bifurcation line $P1$ at which the flow from the two lee-side recirculation bubbles, $Vc6$ and $Vc7$, meet. The flow at this line stagnates leading to a high surface pressure as shown in Fig. 6.c. This line extends to behind the back wheels as shown in Fig. 9.d.

Separated flows from the top-side, the lee-side and the back side faces of the bus merge together to form a strong swirling flow in the wake. This swirling flow extends for a long distance in the wind tunnel behind the bus.

5.2 Instantaneous flow

The instantaneous data from the DES are used to explore the flow structures and the time analysis of the aerodynamic coefficients. Figure 10 shows the isosurface of the positive second invariant of the velocity gradient tensor $Q = -1/2\partial u_i/\partial x_j \partial u_j/\partial x_i$ [16]. This technique as it is describe by Jeong and Hussain [16] is the best technique to track the vortices in the instantaneous flow. The figure then shows the vortical structure around the bus at one instant in time. If we compare the top-side vortices, $V1$ and $V2$ from Fig. 10 to the time-averaged vortices $Vc3$ and $Vc1$ in Fig. 8 we find that the instantaneous slow structures above the bus in the first two third of the bus length is steady while it is highly unsteady on the last one third of the bus length as shown by the unsteady vortices $V1'$.

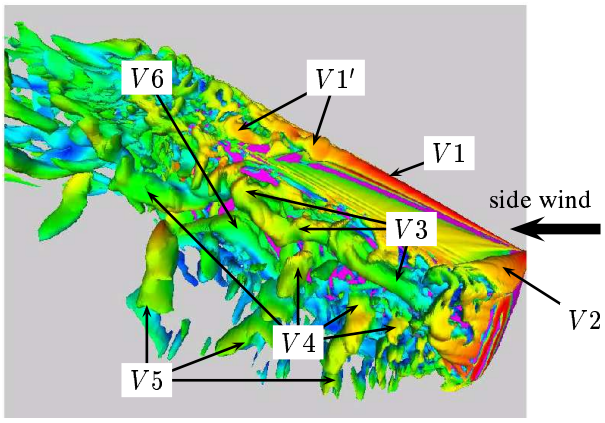

Figure 10: Isosurface of the positive second invariant of the velocity gradient tensor, $Q = 8000$, representing the instantaneous flow structures around the bus.

The instantaneous flow structures in the lee-side flow are completely different from that in the time-averaged flow. However, there are still some vortices that are similar to the time-averaged ones. Vortices $V3$, $V6$ and $V5$ in Fig. 10 are similar to the vortices $Vc6$, $Vc7$ and $Vc8$ in Fig. 9, respectively. Vortices $V5$ in Fig. 10 are due to the flow from the wheel houses. Snapshots similar to Fig. 10 (not shown here) show that the vortices that start at the front wheel house is weaker than that at the back wheel house. They break up and move with the flow towards the vortices generated by the back wheel house. Due to the interaction between vortex $V2$ and vortex $V3$ other secondary vortices $V4$ generate as shown in Fig. 10. The direction of the axes of these vortices is perpendicular to the surface of the bus. Once these vortices have been generated at the front-top edge of the lee-side face, they have been convected away by the free stream flow.

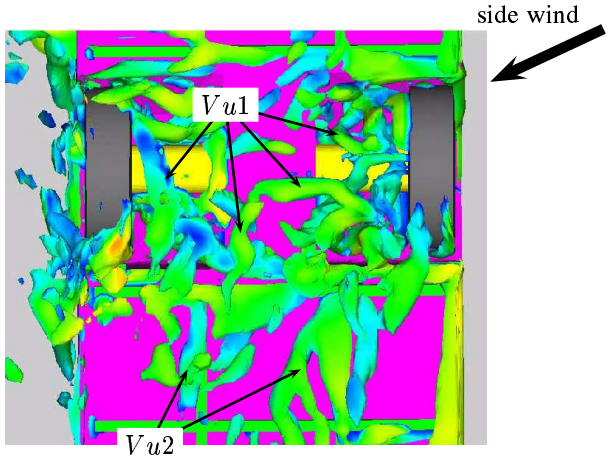

Figure 11: Isosurface of the positive second invariant of the velocity gradient tensor, $Q = 12000$, representing the instantaneous flow structures around the front wheel house.

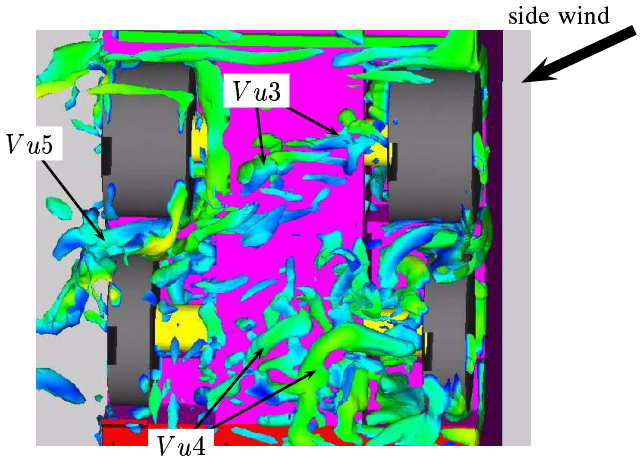

Figure 12: Isosurface of the positive second invariant of the velocity gradient tensor, $Q = 12000$, representing the instantaneous flow structures around the back wheel house.

Figures 11 and 12 show the instantaneous flow structures around and under the wheel house for the front and the back wheels respectively. Many small size vortices shed from the front and the back wheels. The flow structures around the front wheel are similar to the flow structures around the back wheel in the back wheel house where elongated vortices ($Vu2$ in Fig. 11 and $Vu3$ in Fig. 12) with axes parallel to the bottom face of the bus are shed to the lee-side flow. Similar flow structures are found behind the beams in the bottom of the bus as shown by the vortices $Vu2$ in Fig. 11. The flow structures around the front wheel in the back wheel house is different. Instanta-

neous flow structures similar to that of Fig. 12 show that the front wheel in the back wheel house sheds vortices, $Vu3$ in Fig. 12, in a regular fashion to the lee-side flow. The axes of these vortices are perpendicular to the bottom side of the surface of the bus. They merge together once they reach the similar wheel on the other side of the bus to form the big size vortices $Vu5$. The axes of the vortices $Vu5$ is no longer perpendicular to the bottom side of the surface of the bus but parallel to the floor instead. These vortices are the the ones shown in Fig. 10 as $V5$. The time-averaged structures obtained from these vortices result in the vortex $Vc8$ shown in Fig. 8.

The $12mm$ diameter pipes connected to the two sides of the wheel house inject flow in the lee-side flow. These injected flows act as active flows that destroy the formation of the lower side circulation bubble in the lee-side flow. Figure 13 shows a plane passing through these pipes colored by the velocity magnitude. The flows, $F1$, shown in Fig. 13 is coming from these pipes. Snapshots, similar to the one in Fig. 13 show that the direction of these flows are changing with time. This change in the flow direction generates small vortices in the lee-side flow. They are convected away from the surface of the bus to the far wake flow by the mean flow.

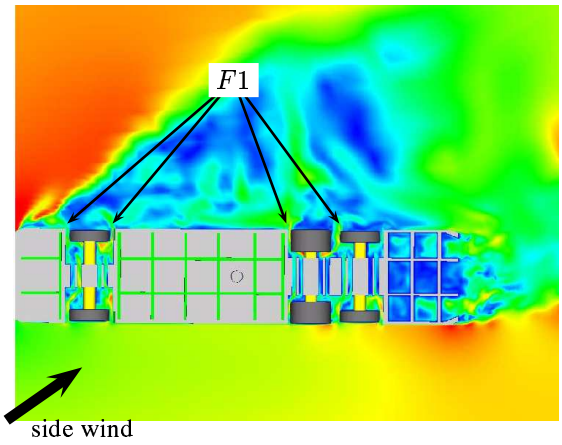

Figure 13: Horizontal plane, passing through the center lines of the small pipes connecting the two sides of the wheel houses, colored with the instantaneous velocity magnitude.

6 Conclusion

DES was successfully made for a side-wind flow around a realistic bus model at a high Reynolds number of 1.3×10^6, based on the speed of the relative side wind and a reference length of $\sqrt{0.1}$ [m]. The time-averaged aerodynamic coefficients were obtained and compared with the experimental values. The side-force and the yaw-moment coefficients agree well with the experimental values while some discrepancies were found for the lift-force and the drag-force coefficients. In all cases, the measured values for the aerodynamic coefficients are in between the minimum and maximum values of the computed coefficients during the sampling time.

Different visualization techniques have been used to visualize the flow structures around the model in both the time-averaged and the instantaneous flows. Comparison between the flow structures in the time-averaged flow and the flow structures in the instantaneous flow shows the following features:

1- The flow separates on the top-side face of the bus forming separation bubbles. These bubbles are stable in the first two third of the bus length while they are more unsteady in the last third of the bus length.

2- The flow in the lee-side face of the bus is completely unsteady and dominated with three-dimensional vortices shed from the upper and the lower edges as well as the front edge of the lee-side face of the bus.

3- The flow under the neath of the bus is dominated with very small structures shed from the geometric details under the bus.

4- The wheel houses inject flows to the lee-side flow. These flows come from the small pipes drilled on the chassis of the bus that connect the two sides of the wheel houses at the front and back axles. They act as the so-called flow control that destroy the formation of the lower part of the recirculation bubble in the lee-side flow.

5- Small unsteady structures are formed in the near wake behind the bus. These structures are shed from the separation bubbles at the edges of the back face. The time-averaged shape of these structures is an upside down arch shape vortex.

6- All the structures around the bus merge together in the wake behind the bus to form a strong swirling flow downstream the wind tunnel in the direction of the free stream flow.

Acknowledgements: The research was supported by the Swedish Agency for Innovation System (VINOVA), Scania, Bombardier Transportation and FLUENT Sweden. Computer time on HELIOS, the Linux cluster provided by C3SE at Chalmers university are gratefully acknowledged. The authors are grateful to professor Lars Davidson for valuable discussions.

References:

[1] T. W. Chiu and L. C. Squire. An experimental study of the flow over a train in a crosswind at large yaw angles up to 90°. *Journal of Wind Engineering and Industrial Aerodynamics*, 45:47–74, 1992.

[2] M. Suzuki, K. Tanemoto, and T. Maeda. Aerodynamic characteristics of train/vehicles under cross winds. *Journal of Wind Engineering and Industrial Aerodynamics*, 91:209–218, 2003.

[3] H. Hemida, S. Krajnović, and L. Davidson. Large-eddy simulations of the flow around a simplified high speed train under the influence of a cross-wind. In *17th AIAA Computational Fluid Dynamics Conference*, Toronto, Ontario, CANADA 6-9 Jun, 2005.

[4] H. Hemida and S. Krajnović. Numerical study of the unsteady flow structures around train-shaped body subjected to side winds. In *European Conference on Computational Fluid Dynamics ECCOMAS CFD 2006*, Egmond aan Zee, The Netherlands, 5-8 September, 2006.

[5] H. Hemida and S. Krajnović. LES study of the impact of the wake structures on the aerodynamics of a generic ice2 train subjected to a side wind. In *The Fourth International Conference on Computational Fluid Dynamics*, Ghent, Belgium, 10-14 July, 2006.

[6] C.J. Baker, J. Jones, F. Lopez-Calleja, and J. Munday. Measurements of the cross wind forces on trains. *Journal of Wind Engineering and Industrial Aerodynamics*, 92:547–563, 2004.

[7] C.J. Baker. Some complex applications of the wind loading chain. *Journal of Wind Engineering and Industrial Aerodynamics*, 91:1791–1811, 2003.

[8] O. Esra and O. Bedii. Turbulent structure of three-dimensional flow behind a model car: 2. exposed to crosswind. *Journal of Turbulence*, 5:1–18, 2004.

[9] W. H. Hucho and G. Sovran. Aerodynamics of road vehicles. *Annual Review of Fluid Mechanics*, 25:483–537, 1993.

[10] C. J. Baker and S. Reynolds. Wind-induced accidents of road vehicles. *Accident Analysis and Prevention*, 24(6):559–575, 1992.

[11] T. Kobayashi and K. Kitoh. Cross-wind effects and the dynamics of light cars. *International Journal of Vehicle Design,Technological Advances in Vehicle Design Series, SP3, Impact of Aerodynamics on Vehicle Design*, pages 142–157, 1983.

[12] J. Petzäll, P. Albertsson, T. Falkmer, and U. Björnsting. Wind forces and aerodynamics: contributing factors to compromise bus and coach safety? *International Journal of Crashworthiness*, 10:435–444, 2005.

[13] Per-Åke Torlund. Experimentell undersökning av sidvindskänsligheten hos en modell av en tvåvåningsbuss i FFA:s vindtunnel LT1. Report (in swedish) FFA TN 2000-05, 1999.

[14] M. Shur, P.R. Spalart, M. Strelets, and A. Travin. Detached-eddy simulation on an airfoil at high angle of attack. In W. Rodi and D. Laurence, editors, *Engineering Turbulence Modelling and Experiments 4*, pages 669–678. Elsevier, 1999.

[15] G.S. Constantinuescu and K.D. Squires. LES and DES investigations of turbulent flow over a sphere at Re=10,000. *Journal of Flow, Turbulence and Combustion*, 70:267–298, 2003.

[16] J. Jeong and F. Hussain. On the identification of a vortex. *Journal of Fluid Mechanics*, 285:69–94, February 1995.